Lung lipid deposition in pneumonias of viral and non-viral aetiology

Potashnikova DM[1;2;3], Tvorogova AV[1;4], Saidova AA[1;3], Sotnikova TN[1], Arifulin EA[4], Lipina TV[3], Shirokova OM[5], Melnikov ES[1], Rodina TA[1], Valyaeva AA[4;6], Zharikova AA[4;6], Zayratyants GO[7], Zayratyants OV[2], Sheval EV[3;4], Margolis LB[8*], Vasilieva EYu[1;2*]

1 City Clinical Hospital Named After I.V. Davydovsky, Moscow Department of Healthcare, Moscow, Russia
2 A.I. Yevdokimov Moscow State University of Medicine and Dentistry of the Ministry of Healthcare of the Russian Federation, Moscow, Russia
3 Department of Cell Biology and Histology, School of Biology, Lomonosov Moscow State University, Moscow, Russia
4 Belozersky Institute of Physico-Chemical Biology, Lomonosov Moscow State University, Moscow, Russia
5 Central Scientific Research Laboratory, Institute of Fundamental Medicine, Privolzhsky Research Medical University, Nizhny Novgorod, Russia
6 Department of Bioengineering and Bioinformatics, Lomonosov Moscow State University, Moscow, Russia
7 City Clinical Hospital Named After S.S. Yudin, Moscow Department of Healthcare, Moscow, Russia
8 National Institute of Child Health and Human Development, NIH, Bethesda MD

* these authors contributed equally

Corresponding author - Vasilieva E.Yu.
Vasilievahelena@gmail.com
City Clinical Hospital Named After I.V. Davydovsky, Moscow Department of Healthcare, 109240, 11/6 Yauzskaya str., Moscow, Russia
A.I. Yevdokimov Moscow State University of Medicine and Dentistry of the Ministry of Healthcare of the Russian Federation,
127473, 20 Delegatskaya str., Moscow, Russia

Keywords: lung pathology; pneumonia; COVID-19; lipid deposition; lipid metabolism

The study was approved by the Moscow City Ethics Committee (protocol № 50/69_13.10.2020) of the Research Institute of the Organization of Health and Healthcare Management and performed according to the Declaration of Helsinki.

Funding
The work was supported by the ANO “William Harvey” and the Russian Science Foundation (grant 21-74-20134). The work of LBM was supported by the NICHD Intramural Program.

Conflict of interest
The authors declare no conflict of interest.

Abstract

Pneumonia is an acute respiratory disease of varying aetiology, which drew much attention during the COVID-19 pandemic. Among many thoroughly studied aspects of pneumonia, lipid metabolism has been addressed insufficiently. Here, we report on abnormal lipid metabolism of both COVID-19- and non-COVID-19-associated pneumonias in human lungs. Morphometric analysis revealed extracellular and intracellular lipid depositions, most notably within vessels adjacent to inflamed regions, where they apparently interfere with the blood flow. Lipids were visualized on Sudan III- and Oil Red O-stained cryosections and on OsO_4-contrasted semi-thin and ultrathin sections. Chromato-mass spectrometry revealed that unsaturated fatty acid content was elevated at inflammation sites compared with the intact sites of the same lung. The genes involved in lipid metabolism were downregulated in pneumonia, as shown by qPCR and *in silico* RNAseq analysis. Thus, pneumonias are associated with marked lipid abnormalities, and therefore lipid metabolism can be considered a target for new therapeutic strategies.

Introduction

Pneumonia encompasses a number of life-threatening conditions that affect the alveoli and distal bronchioli or the interstitial lung tissue and may have various aetiologies, e.g. bacterial, viral, fungal, mycoplasmal, or lipoid. Together with other lower respiratory tract infections, it accounts for over 2.49 million deaths in 2019, with the highest mortality amongst patients older than 70 years (1.23 million deaths), and thus demonstrates the highest mortality rate among infectious diseases [1]. The severity and risk factors depend on pneumonia type and host biology, including immune resistance and tissue resilience [2;3], and are being thoroughly studied. Although a large number of morphological [4;5] and physiological [6;7] abnormalities in inflamed lungs have been reported to date, the specific dysregulations in lipid metabolism associated with lung inflammation of different aetiologies have been addressed much less. This calls for much attention, since lipid synthesis in general, and specifically in lung surfactant, has the key protective role in lung disease [8].

Recently, different aspects of pneumonia have attracted special attention in the context of COVID-19, since the lung is the main target organ for SARS-CoV-2 [9]. The key change in lipid-modulating enzymes for COVID-19 reported to date is the elevation of secreted phospholipase A2 (sPLA2) and its activity in blood plasma [10]. However, whether such systemic abnormalities in lipid metabolism affect the structure of inflamed lung tissue remains obscure. Moreover, it is unknown if these are specific features of lipid metabolism characteristic of COVID-19-associated pneumonia or if they present a general phenomenon.

Here, we addressed these questions by studying lipids in pneumonias of different aetiologies. We used light and electron microscopy of lung specimens with stained (Sudan III, Oil Red O) or contrasted (OsO_4) lipids to reveal the patterns of lipid distribution in different pneumonias and in the inflamed lung vs. the intact lung. Additionally, we used chromato-mass spectrometry of fatty acids and assessed the expression of key enzymes of lipid metabolism *in silico* (by RNA-seq database analysis) and and directly on autopsy specimens (by qPCR) to compare pneumonias of different aetiologies and non-inflamed lungs.

We found that, irrespective of COVID-19 status, the lipids in inflamed lung tissue were deposited as droplets in cell cytoplasm, in extracellular space, and within the small blood vessels. The lipid droplets were mostly located inside cells around the vessels or in their vicinity. Lipids were deposited predominantly in the inflamed areas rather than in non-inflamed areas of the same lung and were not deposited in control intact lung tissue. Deposition of lipids was associated with elevated levels of unsaturated fatty acids and decreased expression of the enzymes involved in lung lipid metabolism.

Materials and methods

The study was approved by the Moscow City Ethics Committee (protocol № 50/69_13.10.2020) of the Research Institute of the Organization of Health and Healthcare Management and performed according to the Declaration of Helsinki.

Autopsies and post-mortem sampling

The study included lung autopsies from 23 patients who died of COVID-19-associated pneumonia (obtained from the department of pathology of the City Clinical Hospital named after S.S. Yudin re-profiled for COVID-19 autopsies according to the international and Russian requirements for working with COVID-19) and 18 patients who died of pneumonias of other aetiologies (obtained from the City Clinical Hospital named after I.V. Davydovsky). Additionally, 10 lung autopsies were taken from individuals without pneumonia (obtained from the City Clinical Hospital named after I.V. Davydovsky). The autopsy data are provided in Supplementary Table 1.

Histological specimens

For the pneumonia lung autopsies, two 1.0x1.5x0.5 cm tissue specimens were taken from the area with macroscopically distinct inflammation, and the other two – from the macroscopically intact area in the upper lobe of the same lung. The latter served as an internal control for morphological examination and lipid content analysis. For the non-pneumonia lung autopsies, two specimens were obtained from one site – the macroscopically intact lung tissue that served as an external control.

The specimens were fixed in 10% buffered formalin. One was used to make cryosections for Sudan III histochemical staining and Oil Red O/anti-CD31/DAPI fluorescence staining. The other was dehydrated according to the standard protocol, cast in paraffin blocks and used for H&E-stained (hematoxylin and eosin) sections.

All dyes for histological stainings were provided by Labiko (Russia). Stainings were performed according to the manufacturer's protocols. Paraffin sections 3-4 μm thick were made according to standard procedures, stained with H&E, dehydrated, and mounted in Vitrogel (Biovitrum, Russia).

For Sudan III staining, cryosections 7 μm thick were made, using a Leica CM1850 cryotome at –25°C. Cryosections were placed on Superfrost Plus glass slides (Thermo Scientific, US) and dried at +60°C. The specimens were stained with Sudan III by Herxheimer, co-stained with Carazzi hematoxylin (exposure 40 s with three rinses in tap water) and mounted in glycerol.

We imaged the histological sections using a Leica DM2000 microscope and a Leica DFC7000 T camera.

Pathological analysis on semi- and ultrathin sections

Tissue specimens 2x2x2 mm in size were obtained from the inflamed site (in pneumonia specimens) or from intact lung tissue (in non-pneumonia specimens) fixed in 2.5% glutaraldehyde (Ted Pella, US) in cacodylate buffer, post-fixed in 1% OsO_4, dehydrated in ethanol and propylene oxide (Sigma-Aldrich, US), and embedded in Epon (Fluka). We obtained semi-thin sections (0.5 µm thick) with a Leica ultramicrotome using glass knives and stained them on glass slides using methylene blue/azure II [11] or polychromatic Twort's staining [12]. After washing in distilled water, the sections were air-dried and mounted in Epon resin under a coverslip. We imaged the specimens using a Leica DM2000 microscope and a Leica DFC7000 T camera.

Ultrathin sections were made with a diamond knife and mounted on slot grids (Ted Pella, US). We stained sections with uranyl acetate and lead nitrate, and examined them using a JEM-1400 electron microscope (Jeol, Japan) at an accelerating voltage of 80 kV.

Morphological and morphometrical analysis of Sudan III-stained specimens

We assessed 100 consequential images for inflamed and intact Sudan III-stained specimens of pneumonia lungs and for intact lung specimens without pneumonia. The morphological analysis was performed manually and included a blinded examination of 100 images by three independent morphologists. All images were checked for the presence of: 1) intracellular lipid droplets (Sudan III–positive droplets in cell cytoplasm), 2) extracellular lipid droplets (Sudan III–positive droplets in the vessel wall or alveolar intercept), and 3) intra-vessel lipid droplets (Sudan III–positive droplets inside blood vessels with/without erythrocytes). The average number of images containing lipid droplets of either kind was expressed as the percentage of images per specimen.

We performed the morphometrical analysis of Sudan III–positive areas using Image Pro software (Media Cybernetics, US). Twenty images were randomly selected for each specimen. For each image, Sudan III–positive droplets were included in a mask containing pixels by colour. The mask was created

semi-automatically on the basis of operator-chosen pixel colour and manually adjusted to include all Sudan III–positive structures. The resulting ROIs were assessed as area per image.

Fluorescence and immunofluorescence specimens

Cryosections of formalin-fixed lung tissue 7 µm thick were washed in PBS (PanEco, Russia) trice. We used 0.01% Tween20 (Sigma-Merck, Germany) for tissue permeabilization (one hour incubation), followed by three washes in PBS.

We performed endothelial staining using a CD31 antibody (clone WM59, BD Biosciences, US) conjugated with fluorescein isothiocyanate (FITC) at a dilution of 1:100 in a humid chamber at +37ºC for one hour. Oil Red O (Sigma-Merck, Germany) dye was further used for staining lipids, (20 min incubation according to the manufacturer's protocol). Nuclei were co-stained with diamidino-2-phenylindole (DAPI) (Thermo Scientific, US) at a final concentration of 1 µg/ml.

Fluorescence imaging was performed in scanning mode on an inverted Zeiss AxioObserver (Zeiss, Germany) fluorescence microscope operating under Zen 3.1 Blue Edition software with a ×40/Oil objective using Hamamatsu ORCA-Flash4.0 V2 (Hamamatsu Photonics, Japan). To visualise the Oil Red O, anti-CD31-FITC and DAPI we used standard Ex.630 nm/Em.670 nm, Ex.488 nm/Em.520 nm, and Ex.405 nm/Em.430 nm filter cubes. We analysed images using ImageJ software (NIH).

Fatty acid profiling by chromato-mass spectrometry

To determine the fatty acid profile, 10 pneumonia lung specimens (COVID-19-associated or non-COVID-19-associated) were analysed. One tissue section was taken from the area with macroscopically distinct inflammation, another was taken from the macroscopically intact area of the same lung. Lung tissue was finely cut, aliquoted and weighed, then stored at -40°C prior to analysis. One aliquot was used to determine the moisture content of the sample as the weight loss on lyophilization, another aliquot was used to determine the fatty acid profile.

Samples were thawed and homogenised with glass beads. We extracted lipids using the Folch method [13]. Briefly: 20 parts (vol.) of a chloroform–methanol mixture (2:1) and 1 part (vol.) of water were added to the sample, followed by 30 s vortexing and 10 min centrifugation at 13000 *g*. The organic

layer was taken and evaporated in a stream of nitrogen. Sodium methoxide and boron trifluoride in methanol were added to the residue to obtain fatty acid methyl esters. We determined the content of 31 fatty acids by means of chromato-mass spectrometry using a gas chromatograph mass spectrometer Shimadzu TQ8050 (Japan). We used chemical ionization with ammonia [14]. Chromatographic separation was performed using a DB-23 column (60 m, 0.25 mm, 0.15µm, 122-2361 Agilent, US). Fatty acids were identified based on the retention times of analytes and on the fragmentation reactions of quasimolecular ions of carboxylic acid ethyl esters and/or their adducts with ammonia [14]. The total mass of fatty acids in the sample and their mass fractions were also calculated.

RNA extraction and reverse transcription

For total RNA extraction, one 5x5x5 mm section was obtained either from the inflamed lung (in pneumonia specimens) or from intact lung (in non-pneumonia specimens), and stored at -20°C in RNAlater (Invitrogen, US). We mechanically disrupted the tissue from RNAlater in a MediMachine (BD Biosciences, US) in 700 µL of RLT buffer (Qiagen, Germany) supplemented with 1% β-mercaptoethanol (Merck, Germany). The volume of suspension was adjusted to 1.5 mL with nuclease-free water. Samples were incubated for 50 min at 54°C with proteinase K (Thermo Scientific, US) at final concentration of 200 µg/mL, then centrifuged for 10 min at 10000 *g*. The supernatant was processed according to the RNeasy mini kit protocol (Qiagen, Germany). DNA was eliminated by on-column digestion using RNase-free DNase (Qiagen, Germany). Total RNA was eluted in 200 µL of nuclease-free water, and stored at 20°C.

We reverse-transcribed cDNA from the total RNA using the ImProm II Kit (Promega, US) with Random primers, according to the manufacturer's instructions.

Real-time qPCR

We detected SARS-CoV-2 RNA in total RNA specimens after extraction using TaqMan qPCR. The primers and probes are listed in Supplementary Table 2. For each sample, amplification of two different regions of the SARS-CoV-2 nucleocapsid gene (*N2* and *N3*) was analysed using primers described earlier [15]. The RNA solution (5 µl per well) was mixed with 5 µl of primer/probe mix and 10 µl of

either qScript XLT One-Step RT-qPCR ToughMix (Quantabio, US) or OneTube RT-PCRmix (Eurogene, Russia).

The genes involved in lipid metabolism included lipases (*LPL, PLA2G4A, PLA2G2A*), involved in fatty acid remodelling and cyclooxigenases (*COX1, COX2*), driving prostaglandin synthesis and thus prompting the fatty acid transition to inflammation mediators, and were analysed in cDNA specimens. The PCR kit was provided by Syntol (Russia). The primers and probes used are listed in Supplementary Table 3. The relative quantities of target genes were normalised by ubiquitin C (*UBC*) reference gene. We analysed all samples in duplicate using a CFX96 Touch cycler with CFX-Manager software (Bio-Rad, US).

Meta-analysis of bulk and single cell RNA-seq datasets

Published bulk and single-cell RNA-seq data from human COVID-19 lung tissue were re-analysed to identify lipid metabolism genes with altered expression in pneumonia samples compared to healthy controls. The bulk RNA-seq dataset GSE150316 [16] was obtained from the Gene Expression Omnibus (GEO) database. The single-cell RNA-seq data were downloaded from SCovid database [17] as lists of differentially expressed genes, which accumulated datasets from different studies. We used clusterProfiler (version v3.18.1) [18] to perform functional over-representation analysis and focused on Gene Ontology (GO) terms enriched with differentially expressed genes related to lipid and specifically fatty acid metabolism. Briefly, we used keywords “lipid”, “fat”, “triglyceride”, or “cholesterol” to search the enrichment results for the specific GO categories. In case of single-cell RNA-seq data, the REVIGO tool [19] was used to remove redundant GO terms.

Data and code availability

The R code for the single-cell RNA-seq data analysis is deposited at https://github.com/kirushka/covid19_FAT.

Results

Lipid droplets are accumulated within lung cells, in extracellular material and within small vessels, in pneumonia

At the first stage of our study, we analysed 12 post-mortem COVID-19 lung specimens on H&E paraffin and semi-thin sections. The diagnoses were established by qPCR analysis of SARS-CoV-2 RNA before/during hospitalization and additionally confirmed by qPCR of post-mortem lung tissue. Histological examination revealed features corresponding to the exudative or proliferative phases of diffuse alveolar damage (Supplementary Figure S1A-E). Importantly, we found cells with cytoplasmic cavities (Supplementary Figure S1E) and vessels with round holes between erythrocytes (Figure 1A-B). Both seemed to have contained lipid droplets removed during routine FFPE specimen processing upon ethanol dehydration. A careful search of H&E paraffin sections allowed us to find multiple examples of such vessels (Supplementary Figure S2).

To check this hypothesis, we analysed the semi-thin sections contrasted with OsO_4 upon fixation and stained with methylene blue/azure II or polychromatic Twort's stain (Supplementary Figure S3A-B). The colour differentiation between lipid droplets and erythrocytes was not so obvious with Twort's staining compared to methylene blue/azure II: it was thus decided to use methylene blue/azure II-stained specimens to assess lung tissue morphology. The OsO_4-contrasted lipid droplets were clearly visible in the lung: cells and cell remnants in the vicinity of the vessels contained small lipid droplets while large lipid droplets were present in the blood vessels (Figure 1C-F). The cells with lipid droplets, and extracellular lipid droplets, were visible in the majority of specimens (12 and 10 specimens, respectively). In 6 specimens, we found lipid droplets inside blood vessels.

To investigate the detailed organization of the lipid droplets, an electron microscopy study was performed. The lipid droplets were easily detected inside blood vessels; all droplets were homogeneous in structure and were not surrounded by membranes (Figure 1G-H).

The morphologic and morphometric analysis of lipid distribution

To understand the role of lipid droplet accumulation, we assessed their prevalence in the lung tissue using cryosections stained with Sudan III. The specimens of intact (non-pneumonia) lungs (n=3), of COVID-19-associated (n=4), and non-COVID-19-associated (n=4) pneumonias were analysed.

The non-pneumonia lungs predominantly did not stain with Sudan III (Figure 2A) or only contained single Sudan III-positive cells (Figure 2B) and rare extracellular droplets. No intra-vessel lipid droplets were detected in non-pneumonia specimens. For each pneumonia, two specimens were analysed: inflamed and macroscopically intact lung tissue. In the inflamed lung, as with the semi-thin sections, the lipid droplets were visible inside cells, in the alveolar and vessel walls, and inside blood vessels in COVID-19-associated (Figure 2C-E) and non-COVID-19-associated pneumonias (Supplementary Figure S4A-C),

The average occurrence of lipid droplets with different localizations was calculated as percentage of frames analysed (Supplementary Table S4; Figure 2F). The differences were statistically significant for all pneumonia specimens from the inflamed area vs. non-pneumonia lung specimens (Mann-Whitney test, $p<0.05$). No significant differences were observed for COVID-19–associated and non-COVID-19–associated pneumonia specimens or for inflamed and intact areas of the same lung. Thus, the prevalent type of lipid distribution was inside cells for specimens with different types of pneumonia and uninfected lungs, while the intra-vessel lipid droplets were characteristic of pneumonia lung tissue.

The morphometric analysis of lipid droplets allowed more distinction between normal lungs and pneumonias (Supplementary Figure S5). The individual specimens within the groups of non-pneumonia lungs, intact pneumonia lungs, and inflamed pneumonia lungs did not differ significantly (1-way ANOVA, Dunns post-test), hence the data from individuals were pooled in their respective groups for further analysis. The differences between all groups were statistically significant (Mann-Whitney test, $p<0.05$) (Figure 2G).

Thus, morphometric analysis allowed us to estimate the total area of lipid droplets in the image and to propose morphometric criteria to assess lung damage via the lipophilic staining.

Fluorescence lipid visualization

To facilitate the further morphometric assessment of lipid distribution in the lung tissue we worked out a protocol of triple fluorescence staining of lung cryosections. The lipids were stained with Oil Red O that was combined with intracellular anti-CD31 and DAPI staining. The detergent concentration and the incubation time were adjusted so that the intra-vessel lipid droplets were not lost during processing. As with the previously used methods, the lipid droplets were visible inside cells, in the alveolar and vessel walls, and inside blood vessels (Figure 3A–C). Thus, we detected the lipid droplets in lungs by three independent light microscopy methods.

The lipid content is altered in pneumonia

To associate the morphologic changes with lipid content alterations in the lung, chromato-mass spectrometry was performed. The non-parametric Wilcoxon test was used for pairwise comparisons of inflamed vs. intact pneumonia lung specimens. The total fatty acid content was not significantly changed (Figure 4A). However, the unsaturated to saturated fatty acids content ratio (U/S ratio) was significantly increased in the specimens with inflammation. We found statistically significant differences in the content of 9 fatty acids in samples from inflamed lung sites compared with intact lung sites (Figure 4B).

GO analysis

To predict the metabolic processes which, upon alteration, may cause the lipid accumulation in lung tissue, we employed Gene Ontology (GO) analysis of the available RNA-seq datasets. The bulk lung COVID-19 RNA-seq datasets as well as single-cell datasets were analysed. The bulk analysis included 9 independent cases and the data on the cumulative dataset. The alterations were found in a number of gene clusters, including those specified by GO terms “regulation of lipid biosynthetic process” and “positive regulation of lipid biosynthetic process” (for the cumulative dataset); “fat cell differentiation” (for 6 of 9 cases) and “regulation of lipid metabolic process” (for 5 of 9 cases). Importantly, the overall trend for gene downregulation was observed, despite the inter-specimen variability (Supplementary

Figure S4A). At the single-cell level, the downregulation of certain genes in lipid metabolic pathways was confirmed: the downregulated genes in lung tissue are mostly assigned to fibroblasts, macrophages and T-cells (Supplementary Table S5). Among the downregulated genes in macrophages and endothelial cells we found those involved in free fatty acid/cholesterol uptake, storage, and metabolism.

RT-qPCR

The selected array of genes confirmed the data on the downregulation of genes involved in lipid metabolism. *PLA2G2A*, *COX2* and *LPL* were generally detected at very low levels in the lungs and showed no significant differences in expression between pneumonias and normal lungs (data not shown). *PLA2G4A* was downregulated in pneumonias of both types compared with normal lungs (Supplementary Figure S4B). *COX1* was downregulated in non-COVID-19-associated pneumonias (Supplementary Figure S4C).

Discussion

Studies of pneumonia have a long history. It is well-established that although pneumonia may be caused by various pathogens, the most common aetiological agents for this disease are bacteria and viruses. Bacteria-induced pneumonias were described in the 30s-50s of the 19th century [20;21], while virus-induced pneumonias were studied in the 30s-40s of the 20th century [22-24]. Deteriorations of lung tissue were thoroughly studied for over a century and a number of pneumonia type-specific alterations were found [2;25;26]. Among multiple pathologic processes associated with pneumonia, lipid metabolism remains the least studied. The recent COVID-19 pandemic significantly increased pneumonia incidence and triggered a new wave of publications on this disease [27;28]. A few of these publications used the above-mentioned techniques to reveal lipid deposition. In particular, light microscopy analysis of the damaged lung [29;30] revealed the cytoplasm foaming of the infected cells. One paper described lipid droplets in the interalveolar space and inside the small lung vessels of COVID-19 patients with symptoms of obesity [31]. The authors attribute this to SARS-CoV-2 infection of adipocytes. In our sample set, we observed similar droplets in obese and non-obese patients.

It remains to be understood whether lipid dysregulation results in local/systemic lipid metabolism alterations and whether they are COVID-19-specific or are a part of general pneumonia-associated pathology. Here, we attempted to answer these questions.

The scarcity of lipid studies is, in part, due to the fact that paraffin sections are unsuitable for lipid-rich structures' analysis. To reveal the lipid deposits, one has to use cryosections stained with lipophylic dyes (Sudan III, Sudan Black, etc.) and semi-thin sections with OsO_4 post-fixation, which stabilizes the lipid-rich structures [32]. Along with these methods, we developed a protocol of fluorescence staining that reveals both lipids (stained with Oil Red O) and cellular antigens. Furthermore, we performed the EM analysis of the ultrathin sections of the inflamed lung tissue. These methods enabled us to reveal the morphological alterations caused by pneumonias. We analysed lung specimens from 12 post-mortem cases with diagnosed COVID-19 pneumonia on semi-thin specimens. Additionally, we analysed 8 pneumonia specimens (4 COVID-19 and 4 non-COVID-19) and 3 non-pneumonia specimens on Sudan III-stained cryosections.

We identified homogeneous lipid droplets with no surrounding membranes at different sites. The prevailing site of droplet localization was cell cytoplasm regardless of pneumonia aetiology. Less common was extracellular localization of the droplets (in the vessel wall or alveolar intercept). Finally, in some patients, large lipid droplets appeared in blood vessels, almost blocking the blood flow.

We have quantified the occurrence for all kinds of lipid deposition. The intra-vessel lipid droplets were located predominantly in the inflamed lung area. The non-inflamed lung areas from the same individuals contained fewer intra-vessel droplets, although the difference was not statistically significant. Importantly, the intra-vessel lipid droplets were totally absent in the non-inflamed lungs of individuals who died of causes unrelated to pneumonia. Thus, the lipid droplets in the blood flow are indicative of pneumonia regardless of its aetiology.

The morphometric analysis of lipid deposition regardless of its localization revealed the statistically significant differences between non-pneumonia lungs, intact regions of pneumonia lung and inflamed regions of pneumonia lung. Such differences imply that the major structural abnormalities of lipid

deposition are limited to the inflammation region, although the macroscopically intact area of pneumonia lung is also altered and cannot be considered normal.

Chromato-mass spectrometry revealed a significant shift towards unsaturated fatty acids in inflamed lung areas compared with non-inflamed parts of the same lung, confirming that lipid abnormalities are local. Some insight into the crosstalk of inflammation and lipid metabolism was provided via the macrophage function [33;34]: macrophage activation *in vitro* resulted in metabolic shifts and enhanced fatty acid synthesis. However how the changes in lipid metabolism lead to the lipid deposition remains to be understood. It may be related to the altered activity of genes encoding for lipid metabolism enzymes, as evaluated from RNA-seq analysis and qPCR data. Also, lipid accumulation in pneumonia may result from tissue decomposition in the inflamed areas and of the macrophages' inability to eliminate the accumulated lipids.

These data are in general agreement with the published results on the lipid level changes in bronchoalveolar lavage fluids associated with ARDS and pneumonia [35;36]. Indeed, the decrease in saturated C16:0 and the increase in unsaturated C18:1 and C18:2 have been reported in pneumonia. The recent COVID-19 studies on plasma lipid levels now allow a comparison of the metabolic effects – restricted to the lung or systemic during infection [37;38]. The link of these data to cell and tissue morphology would provide a complex view on pneumonia pathogenesis. Whatever the mechanisms of lipid accumulation are, lipid deposition in lung vessels, especially in the small ones, seems to be able to alter the blood flow and affect the gas exchange, one of the key aspects of various pneumonias [27;39].

In summary, we demonstrated the lipid depositions in lung tissue with COVID-19- and non-COVID-19-associated pneumonias, adjacent to inflamed regions, and provided morphometrical characteristics of lipid-associated lung damage. Moreover, we report on the elevation of the unsaturated fatty acid content at sites of inflammation compared with the macroscopically intact lung and a general downregulation of lipid metabolic pathways. Together, these data provide new insights into pneumonia

pathogenesis and its association with lipid metabolism and inflammation. Our results indicate that lipids can be considered a target for therapeutic interventional strategy in pneumonia.

Acknowledgements

The authors are grateful to Prof. A.V. Shpektor and Dr. V.N. Manskikh for stimulating discussions and valuable suggestions and to Dr. Barry Alpher for editing the manuscript.

PDM, ShEV – conceived and performed the experiments, analysed the data, provided figures, wrote the manuscript. TAV, SAA – conceived and performed the experiments, analysed the data, provided figures. STN, AEA, LTV, ShOM, MES, RTA – performed the experiments, analysed the data. VAA, ZhAA, ZGO – collected and analysed the data, provided figures and tables. ZOV, MLB, VEYu – conceived the experiments, analysed the data, wrote the manuscript.

Funding

The work was supported by the ANO "William Harvey" and the Russian Science Foundation (grant 21-74-20134). The work of LBM was supported by the NICHD Intramural Program.

Conflict of interest

The authors declare no conflict of interest.

References

1. GBD 2019 Diseases and Injuries Collaborators. Global burden of 369 diseases and injuries in 204 countries and territories, 1990-2019: a systematic analysis for the Global Burden of Disease Study 2019. Lancet 2020; **396(10258)**:1204-1222.
2. Torres A., Cilloniz C., Niederman M.S., et al. Pneumonia. Nat Rev Dis Primers 2021; **7(1)**:25. doi: 10.1038/s41572-021-00259-0.
3. Mizgerd, J.P. Pathogenesis of severe pneumonia: advances and knowledge gaps. Curr Opin Pulm Med. 2017; **23(3)**:193-197. doi: 10.1097/MCP.0000000000000365.
4. Kradin, R. L. & Digumarthy, S. The pathology of pulmonary bacterial infection. Semin. Diagn. Pathol. 2017; **34**:498–509.
5. Pritt, B. S. & Aubry, M. C. Histopathology of viral infections of the lung. Semin. Diagn. Pathol. 2017; **34**:510–517.

6. Quinton, L. J., Walkey, A. J. & Mizgerd, J. P. Integrative physiology of pneumonia. Physiol. Rev. 2018; **98**:1417–1464.
7. Whitsett, J.A. & Alenghat, T. Respiratory epithelial cells orchestrate pulmonary innate immunity. Nat. Immunol. 2015; **16**:27–35.
8. Agudelo, C.W., Samaha, G. & Garcia-Arcos, I. Alveolar lipids in pulmonary disease. A review. Lipids Health Dis 2020; **19**:122. https://doi.org/10.1186/s12944-020-01278-8
9. Valyaeva, A. A., Zharikova, A. A., & Sheval, E. V. SARS-CoV-2 cellular tropism and direct multiorgan failure in COVID-19 patients: Bioinformatic predictions, experimental observations, and open questions. Cell Biology International. 2022; 1– 19.
10. Snider, J.M., You, J.K., Wang, X., et al. Group IIA secreted phospholipase A2 is associated with the pathobiology leading to COVID-19 mortality. J Clin Invest. 2021; **131(19)**:e149236. doi: 10.1172/JCI149236.
11. Cold Spring Harb Protoc 2010; doi:10.1101/pdb.rec12090.
12. Manskikh, V. N. and Sheval, E. V. An Adaptation of Twort's Method for Polychromatic Staining of Epoxy-Embedded Semithin Sections. Histochem Cell Biol 2020; **153(2)**: 121–27.
13. Folch, J., Mark Lees, M., and Sloane Stanley, G.H. A simple method for the isolation and purification of total lipids from animal tissues. J Biol Chem. 1957; **226(1)**:497-509.
14. Schober, Y., Wahl, H. G., Renz H., Nockher, W. A. Determination of red blood cell fatty acid profiles: Rapid and high-confident analysis by chemical ionization-gas chromatography-tandem mass spectrometry. J Chromatogr B Analyt Technol Biomed Life Sci. 2017; **1040**:1-7.
15. Komissarov, A., Molodtsov, I., Ivanova, O., et al. High SARS-CoV-2 load in the nasopharynx of patients with a mild form of COVID-19 is associated with clinical deterioration regardless of the hydroxychloroquine administration. *PLoS One*. 2021; **16(1)**:e0246396.
16. Desai, N., Neyaz, A., Szabolcs, A. et al. Temporal and spatial heterogeneity of host response to SARS-CoV-2 pulmonary infection. Nat Commun 2020; **11**, 6319.
17. Changlu, Q., Chao, W., Lingling, Z., et al. SCovid: single-cell atlases for exposing molecular characteristics of COVID-19 across 10 human tissues, *Nucleic Acids Research* 2022; **50(D1)**: D867–D874.
18. Wu, T., Hu, E., Xu, S., et al. clusterProfiler 4.0: A universal enrichment tool for interpreting omics data. *Innovation (Camb)*. 2021; **2(3)**:100141.
19. Supek, F., Bošnjak, M., Škunca, N., et al. REVIGO summarizes and visualizes long lists of gene ontology terms. *PLoS One*. 2011; **6(7)**:e21800.
20. Laennec, R. T. Translated from the 3rd French ed. by J. Forbes, with notes of Prof. Andral from the 4th ed. New York: SS & Wm. Wood; 1838. A treatise on the diseases of the chest and on mediate auscultation.
21. Rokitansky C. Manual of Pathological Anatomy. London: Sydenham Society; 1852. Inflammations of the lungs (pneumoniae).
22. Rivers, T.M., Berry, G.P. PSITTACOSIS : IV. EXPERIMENTALLY INDUCED INFECTIONS IN MONKEYS. J Exp Med. 1931; **54(1)**:129-44. doi: 10.1084/jem.54.1.129.
23. Meiklejohn, G., Beck, M.D., Eaton, M.D. ATYPICAL PNEUMONIA CAUSED BY PSITTACOSIS-LIKE VIRUSES. J Clin Invest. 1944; **23(2)**:167-75. doi: 10.1172/JCI101480.
24. Eaton, M.D., van Herick, W., Meiklejohn, G. STUDIES ON THE ETIOLOGY OF PRIMARY ATYPICAL PNEUMONIA : III. SPECIFIC NEUTRALIZATION OF THE VIRUS BY HUMAN SERUM. J Exp Med. 1945; **82(5)**:329-42. doi: 10.1084/jem.82.5.329.
25. Ruuskanen, O., Lahti, E., Jennings, L.C., et al. Viral pneumonia. Lancet. 2011; **377(9773)**:1264-75. doi: 10.1016/S0140-6736(10)61459-6.
26. Gill, J.R., Sheng, Z.M., Ely, S.F., et al. Pulmonary pathologic findings of fatal 2009 pandemic influenza A/H1N1 viral infections. Arch Pathol Lab Med. 2010; **134(2)**:235-43. doi: 10.5858/134.2.235.
27. Gattinoni, L., Gattarello, S., Steinberg, I., et al. COVID-19 pneumonia: pathophysiology and management. Eur Respir Rev. 2021; **30(162)**:210138. doi: 10.1183/16000617.0138-2021.

28. Chilosi, M., Poletti, V., Ravaglia, C., et al. The pathogenic role of epithelial and endothelial cells in early-phase COVID-19 pneumonia: victims and partners in crime. Mod Pathol. 2021; **34(8)**:1444-1455. doi: 10.1038/s41379-021-00808-8.
29. Nardacci, R., Colavita, F., Castilletti, C., et al. Evidences for lipid involvement in SARS-CoV-2 cytopathogenesis. Cell Death Dis. 2021; **12(3)**:263. doi: 10.1038/s41419-021-03527-9.
30. Grootemaat, A.E., van der Niet, S., Scholl, E.R., et al. Lipid and Nucleocapsid N-Protein Accumulation in COVID-19 Patient Lung and Infected Cells. Microbiol Spectr. 2022; **10(1)**:e0127121. doi: 10.1128/spectrum.01271-21.
31. Cinti, S., Graciotti, L., Giordano, A., et al. COVID-19 and fat embolism: a hypothesis to explain the severe clinical outcome in people with obesity. Int J Obes (Lond). 2020; **44(8)**:1800-1802. doi: 10.1038/s41366-020-0624-5.
32. Angermüller, S., Fahimi, H.D. Imidazole-buffered osmium tetroxide: an excellent stain for visualization of lipids in transmission electron microscopy. Histochem J. 1982; **14(5)**:823-35. doi: 10.1007/BF01033631.
33. Castoldi, A., Monteiro, L.B., van Teijlingen Bakker, N. et al. Triacylglycerol synthesis enhances macrophage inflammatory function. Nat Commun 2020; **11**, 4107. https://doi.org/10.1038/s41467-020-17881-3.
34. Ecker, J., Liebisch, G., Englmaier, M., et al. Induction of fatty acid synthesis is a key requirement for phagocytic differentiation of human monocytes. Proc Natl Acad Sci U S A. 2010; **107(17)**:7817-22. doi: 10.1073/pnas.0912059107.
35. Zheng, Y., Ning, P., Luo, Q. et al. Inflammatory responses relate to distinct bronchoalveolar lavage lipidome in community-acquired pneumonia patients: a pilot study. Respir Res 2019; **20**, 82. https://doi.org/10.1186/s12931-019-1028-8.
36. Schmidt, R., Meier, U., Yabut-Perez, M., et al. Alteration of fatty acid profiles in different pulmonary surfactant phospholipids in acute respiratory distress syndrome and severe pneumonia. Am J Respir Crit Care Med. 2001; **163(1)**:95-100. doi: 10.1164/ajrccm.163.1.9903029.
37. Nguyen, M., Bourredjem, A., Piroth, L., et al. High plasma concentration of non-esterified polyunsaturated fatty acids is a specific feature of severe COVID-19 pneumonia. Sci Rep. 2021; **11(1)**:10824. doi: 10.1038/s41598-021-90362-9.
38. Kimhofer, T., Lodge, S., Whiley, L., et al. Integrative Modeling of Quantitative Plasma Lipoprotein, Metabolic, and Amino Acid Data Reveals a Multiorgan Pathological Signature of SARS-CoV-2 Infection. J Proteome Res. 2020; **19(11)**:4442-4454. doi: 10.1021/acs.jproteome.0c00519.
39. Marshall, B.E., Hanson, C.W., Frasch, F., et al. Role of hypoxic pulmonary vasoconstriction in pulmonary gas exchange and blood flow distribution. 2. Pathophysiology. Intensive Care Med. 1994; **20(5)**:379-89. doi: 10.1007/BF01720916.

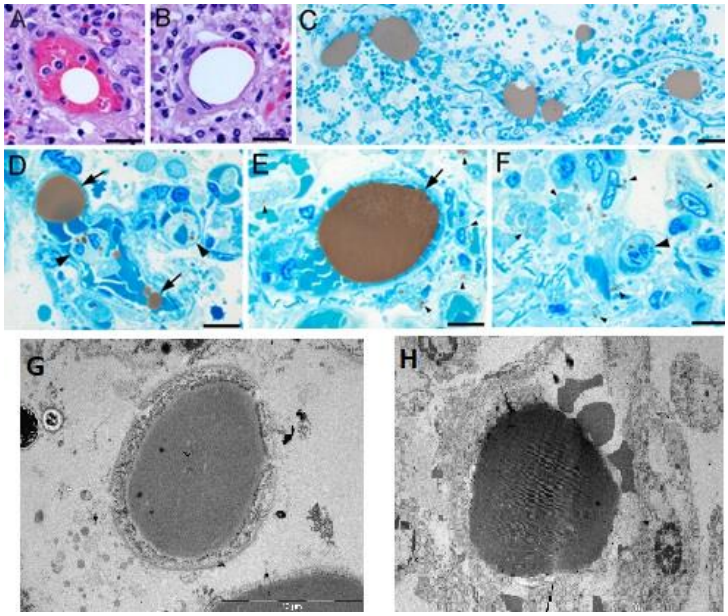

Figure 1. Lipid droplets in COVID-19-associated pneumonia lung. A – paraffin section, hematoxylin & eosin staining. A small vessel contains a round cavity surrounded by erythrocytes. Scale bar – 25 µm. B – paraffin section, hematoxylin & eosin staining. Erythrocytes in a small vessel are deformed and pushed to the vessel wall. Scale bar – 25 µm. C – OsO_4-contrasted lipid droplets inside blood vessels in the lung. Scale bar – 100 µm. D – OsO_4-contrasted lipid droplets are present in the blood vessel (arrows) and in the cells near the vessel (arrowheads). Scale bar – 10 µm. E – OsO_4-contrasted lipid droplet fills the blood vessel (arrow) with erythrocytes pushed to the vessel wall. Cells and cell remnants in the vicinity of the vessel contain smaller lipid droplets (arrowheads). Scale bar – 10 µm. F – OsO_4-contrasted small lipid droplets in the cytoplasm of the lung-infiltrating neutrophil (large arrowhead) and in other intact and destroyed cells (small arrowheads). Scale bar – 10 µm. G – OsO_4-contrasted lipid droplets are homogeneous in ultrathin sections. EM, scale bar – 10 µm. H – a homogeneous OsO_4-contrasted lipid droplet in the blood vessel with erythrocytes, the erythrocytes are pushed to the vessel wall. EM, scale bar – 20 µm.

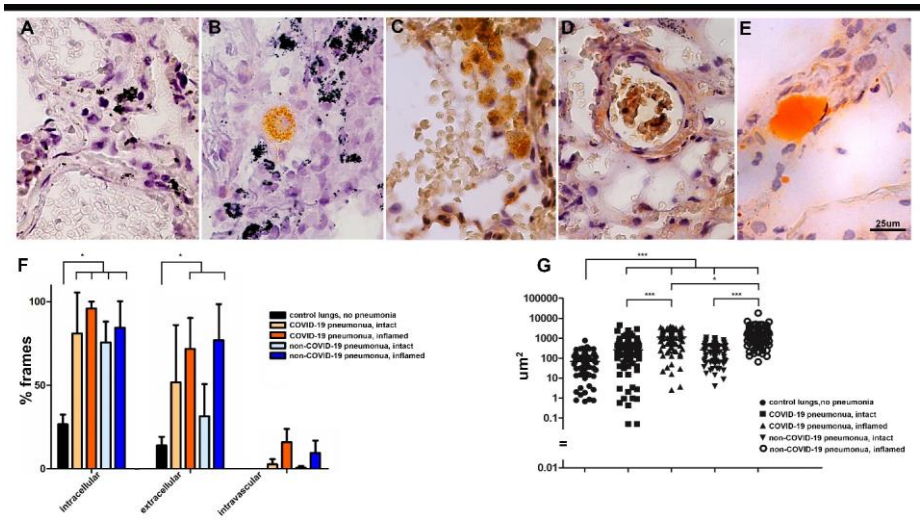

Figure 2. The lipid distribution in non-pneumonia lung tissue and pneumonias of various aetiologies. A – representative non-pneumonia lung tissue staining with Sudan III: no lipid-rich structures are typically present inside blood vessels, in the vessel walls or in the alveolar intercepts. Scale bar – 25 µm. B – representative non-pneumonia lung tissue staining with Sudan III: single cells with lipid-rich cytoplasm in the interalveolar wall present the most common type of Sudan III-positive events in non-pneumonia lung tissue. Example of intracellular lipid deposition. Scale bar – 25 µm. C – representative pneumonia lung tissue staining with Sudan III (COVID-19-associated pneumonia, inflamed area of the lung): grouped cells with lipid-rich cytoplasm are present in the alveolar intercept and in the vicinity of blood vessels. Example of intracellular lipid deposition. Scale bar – 25 µm. D – representative pneumonia lung tissue staining with Sudan III (COVID-19-associated pneumonia, inflamed area of the lung): the blood vessel wall contains lipid-rich structures among the elastic fibers. Example of extracellular lipid deposition. Scale bar – 25 µm. E – representative pneumonia lung tissue staining with Sudan III (COVID-19-associated pneumonia, inflamed area of the lung): blood vessel filled with a lipid droplet. Example of intravascular lipid deposition. Scale bar – 25 µm. F – the occurrence rate of intacellular / extracellular / extravascular lipid deposition in non-pneumonia lung tissue (n=3 specimens), COVID-19-associated pneumonia (n=4 specimens) and non-COVID-19-associated pneumonia (n=4 specimens). Analysis performed on 100 consecutive frames per specimen, occurrence rate determined as percentage of frames containing either type of lipid deposition. Inflamed area of the lung (determined macroscopically) was analysed along with the intact area of the lung (determined macroscopically and obtained from the upper lobe of the same lung) for each pneumonia case. * - statistically significant differences ($p<0.05$, Mann-Whitney test). G – the total area of lipid deposition per frame (μm^2) in non-pneumonia lung tissue (n=3 specimens), COVID-19-associated pneumonia (n=4 specimens) and non-COVID-19-associated pneumonia (n=4 specimens). Inflamed area of the lung was analysed along with the intact area of the same lung for each pneumonia case. Total area of lipid deposition was assessed on 20 random frames per specimen, the data from specimens were pooled in their respective groups for further analysis. * - statistically significant differences ($p<0.05$, Mann-Whitney test); *** - statistically significant differences ($p<0.001$, Mann-Whitney test).

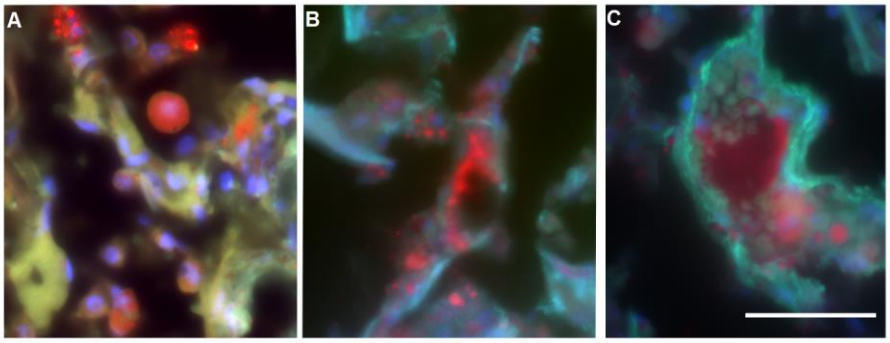

Figure 3. Representative triple fluorescence staining of pneumonia lung tissue with Oil Red O (red)/anti-CD31 (green)/DAPI (blue). Non-COVID-19-associcted pneumonia, inflamed area of the lung. Objective x40/Oil. Scale bar – 50 µm. A – grouped cells with lipid-rich cytoplasm. Example of intracellular lipid deposition. B – lipid-rich structures in the blood vessel wall. Example of extracellular lipid deposition. Objective x40/Oil. Scale bar – 50 µm. C – blood vessel filled with erythrocytes and a lipid droplet. Example of intravascular lipid deposition. Objective x40/Oil. Scale bar – 50 µm.

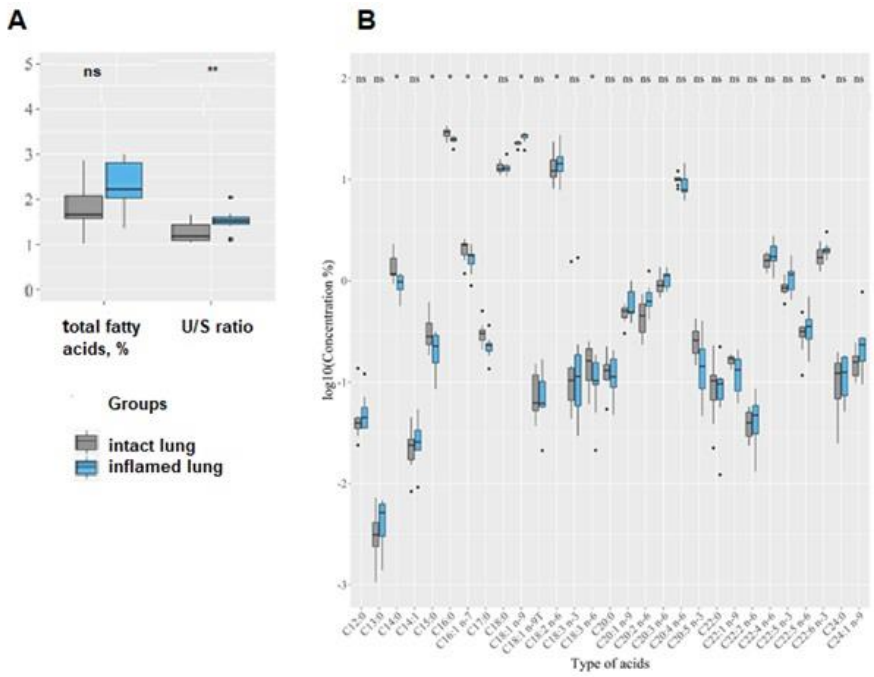

Figure 4. The lipid content of the inflamed vs. intact sections of lung tissue with pneumonia assessed by chromato-mass spectrometry. A – Total fatty acid content in inflamed pneumonia and intact pneumonia lung specimens. The differences are statistically insignificant. The ratio of unsaturated/saturated fatty acids per specimen. The difference is statistically significant (Wilcoxon test, $p<0.01$). B – the log-transformed concentrations of individual fatty acids. The difference is statistically significant for 9 fatty acids (Wilcoxon test, $p<0.05$). The saturated fatty acids C14:0 (tetradecanoic, myristic), C15:0 (pentadecanoic), C16:0 (hexadecanoic, palmitic), and C17:0 (heptadecanoic, margaric), and the unsaturated fatty acids C16:1 n-7 (palmitoleic) and C18:3 n-6 (γ-linolenic) were significantly decreased in the inflamed area of the lung compared with the macroscopically intact area, whereas the unsaturated fatty acids C18:1 n-9 (oleic), C18:2 n-6 (α-linoleic), and C22:6 n-3 (docosahexaeoic) were significantly elevated in the inflamed area of the lung compared with the macroscopically intact area.

Supplementary Figures.

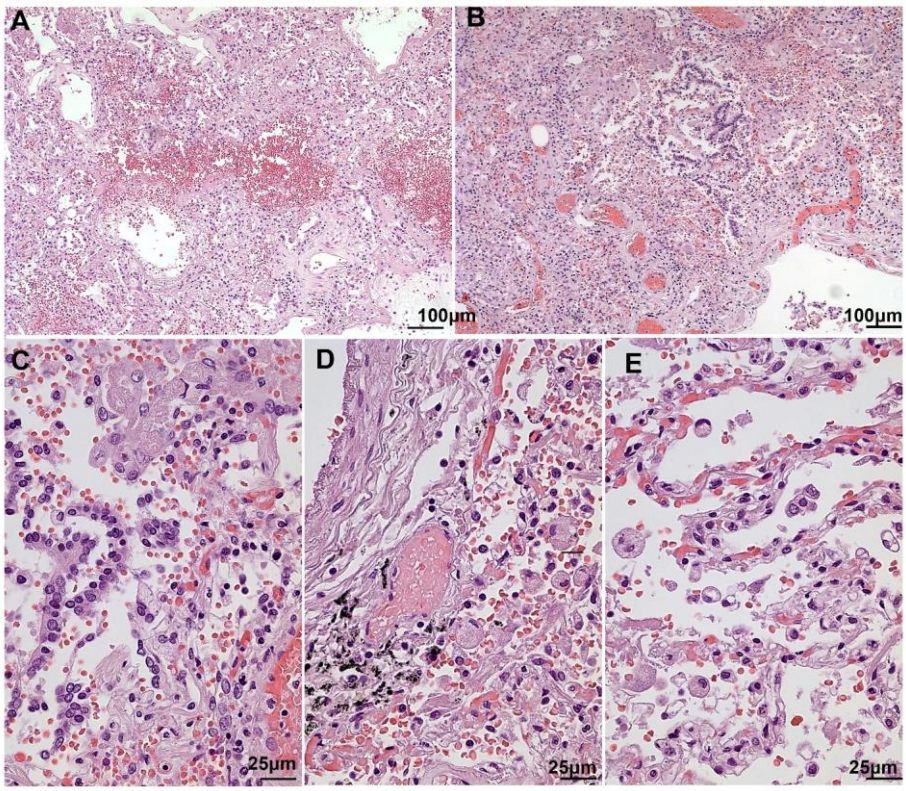

Supplementary Figure S1. H&E paraffin sections of COVID-19-associated pneumonias, characteristic changes of lung tissue morphology. A – exudative stage of diffuse alveolar damage, loss of lung morphology; fields of extravascular erythrocytes within lung tissue. Scale bar – 100 µm. B – proliferative stage of diffuse alveolar damage, loss of lung morphology; alveolar remnants contain proliferating epithelial cells. The blood vessels are filled with erythrocytes; surrounded by the erythrocytes is the cavity that presumably contained a lipid droplet. Scale bar – 100 µm. C –alveolar remnants with giant cells and desquamated proliferating epithelium. Scale bar – 25 µm. D – blood vessels filled with erythrocytes. Characteristic erythrocyte sludges in capillaries. Scale bar – 25 µm. E – apart from erythrocyte sludges in the capillaries, cells with foamed cytoplasm or empty cavities in the cytoplasm are present near the vessels. Scale bar – 25 µm.

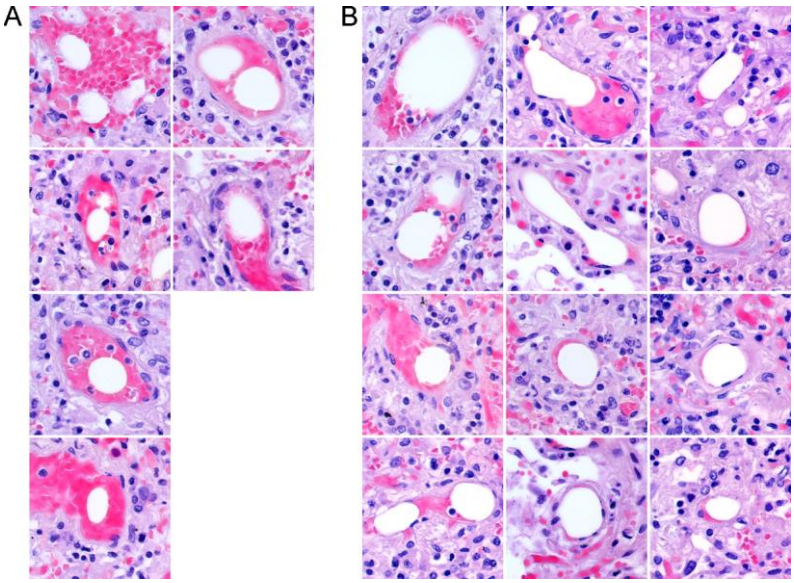

Supplementary Figure S2. The gallery of images obtained upon H&E specimen examination of COVID-19-associated pneumonias. The majority of the blood vessels in pneumonia lungs are filled with erythrocytes. A – a large number of vessels contains cavities, completely surrounded by erythrocytes, that presumably contained lipid-rich structures lost upon specimen dehydration in ethanol. B – other vessels contain deformed erythrocytes pushed to the side of the vessel. The sizes of the cavities are close to the sizes of the small vessels.

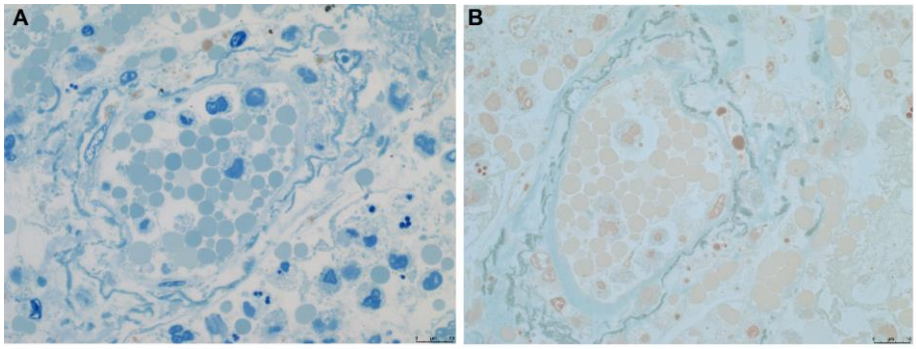

Supplementary Figure S3 Comparison of methylene blue/azure II and Twort's staining of lipid-rich structures in COVID-19-associated pneumonia. A – The major traits of pathological injury of lungs are clearly visible on methylene blue/azure II specimens; the lipid-rich structures in this case have a pale brown colour that allows their distinction from other cellular and extracellular structures, which have a blue colour. B – The colour differentiation between lipid droplets and erythrocytes is not so obvious with Twort's staining: the lipid droplets in this case have a dark brown colour, while the erythrocytes have a pale brown colour.

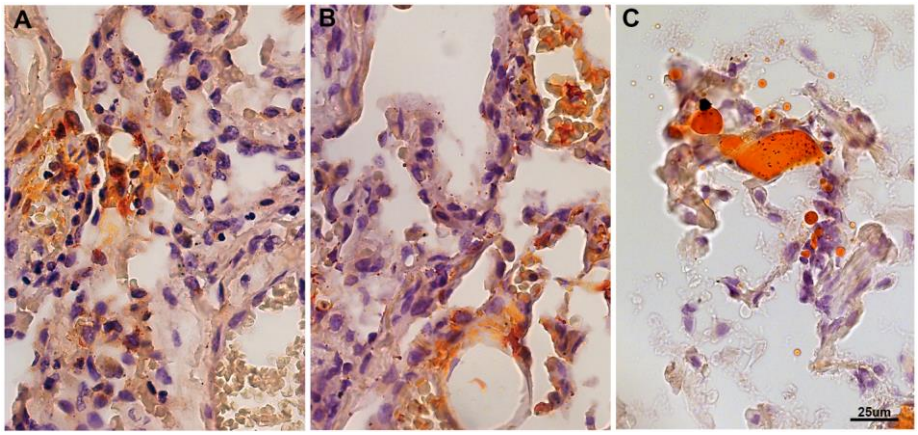

Supplementary Figure S4. The lipid distribution in non-COVID-19-associated pneumonia. A – representative pneumonia lung tissue staining with Sudan III (non-COVID-19-associated pneumonia, inflamed area of the lung): grouped cells with lipid-rich cytoplasm are present in the alveolar intercept and in the vicinity of blood vessels. Example of intracellular lipid deposition. Scale bar – 25 μm. B – representative pneumonia lung tissue staining with Sudan III (non-COVID-19-associated pneumonia, inflamed area of the lung): the blood vessel wall contains lipid-rich structures among the elastic fibers. Example of extracellular lipid deposition. Scale bar – 25 μm. C – representative pneumonia lung tissue staining with Sudan III (non-COVID-19-associated pneumonia, inflamed area of the lung): blood vessel filled with a lipid droplet. Example of intravascular lipid deposition. Scale bar – 25 μm.

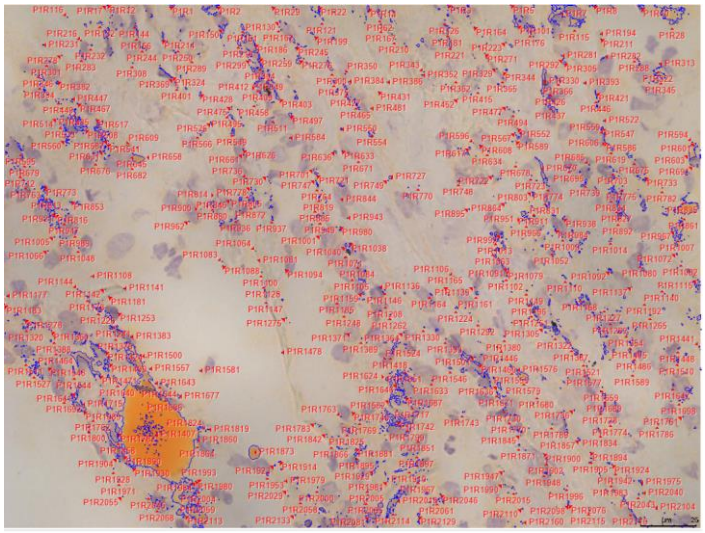

Supplementary Figure S5. Example of the morphometric analysis of Sudan III-stained lung cryosections. ImagePro mask was semi-manually generated according to pixel colour. The total area of the mask was calculated in μm^2. Scale bar – 25 µm.

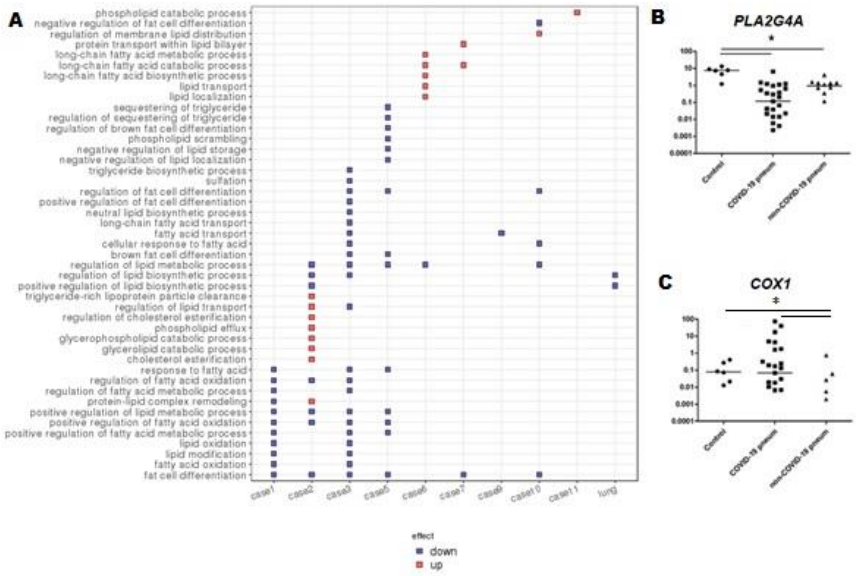

Supplementary Figure S6. GO and qPCR analysis. A - The bulk RNA-seq dataset analysis included 9 independent pneumonia cases (“case1”; “case2”; “case3”; “case5”; “case6”; “case7”; “case9”; “case10”; “case11”) and the data on the cumulative dataset (“lung”). The overall trend for gene downregulation is observed despite the variability between cases. B – Relative normalized gene expression data, *PLA2G4A*, qPCR. * - statistically significant differences ($p<0.05$, Mann-Whitney test). C – B – Relative normalized gene expression data, *COX1*, qPCR. * - statistically significant differences ($p<0.05$, Mann-Whitney test).

Supplementary Table S1. Description of the autopsies included in the study.

Autopsy	Sex	Age	Pneumonia	COVID-19 in-hospital qPCR	COVID-19 post-mortem qPCR	Height/ weight/ BMI
1 COVID-19	F	82	+	NA	+	BMI<30
2 COVID-19	M	79	+	+	+	NA
3 COVID-19	F	68	+	NA	+	BMI≥30
4 COVID-19	F	61	+	+	+	BMI≥30
5 COVID-19	M	79	+	+	+	NA
6 COVID-19	M	62	+	+	+	NA
7 COVID-19	M	73	+	+	+	BMI≥30
8 COVID-19	M	79	+	+	+	BMI≥30
9 COVID-19	F	78	+	-	+	BMI<30
10 COVID-19	M	73	+	-	+	BMI<30
11 COVID-19	M	89	+	+	+	BMI≥30
12 COVID-19	M	74	+	+	+	BMI<30
13 COVID-19	F	84	+	+	+	BMI<30
14 COVID-19	F	70	+	+	NA	BMI<30
15 COVID-19	M	84	+	+	NA	BMI<30
16 COVID-19	F	67	+	+	NA	180/80/24,7
17 COVID-19	M	62	+	-	+	BMI<30
18 COVID-19	M	61	+	-	+	169/44,6/15,6
19 COVID-19	F	87	+	NA	+	BMI<30
20 COVID-19	M	71	+	-	+	BMI<30
21 COVID-19	M	71	+	-	+	NA/NA/NA
22 COVID-19	F	63	+	-	+	169/90/31,5
23 COVID-19	F	80	+	NA	+	BMI<18.5
1 non-COVID-19	M	54	+	-	-	187/87/24,8
2 non-COVID-19	M	67	+	-	-	BMI<30
3 non-COVID-19	M	40	+	-	-	170/95/32,8
4 non-COVID-19	F	76	+	-	-	BMI<30
5 non-COVID-19	F	47	+	-	-	175/86/28
6 non-COVID-19	M	61	+	-	-	BMI<30
7 non-COVID-19	M	89	+	-	-	BMI<30
8 non-COVID-19	F	89	+	-	-	160/50/19,5
9 non-COVID-19	F	73	+	-	-	170/80/28
10 non-COVID-19	M	89	+	-	-	165/60/22
11 non-COVID-19	M	75	+	-	-	180/75/23,1
12 non-COVID-19	M	82	+	-	-	BMI<30
13 non-COVID-19	M	81	+	-	-	180/80/24,6

Отформатировано: Шрифт: 12 пт

14 non-COVID-19	F	59	+	-	-	BMI<18.5
15 non-COVID-19	F	80	+	NA	-	165/92/33,7
16 non-COVID-19	F	62	+	NA	-	168/105/37,2
17 non-COVID-19	F	61	+	-	-	164/76,6/28,4
18 non-COVID-19	M	68	+	NA	-	182/84/25,3
1 Ctrl	F	95	-	NA	-	BMI<30
2 Ctrl	M	90	-	NA	-	BMI<30
3 Ctrl	F	74	-	NA	-	BMI<30
4 Ctrl	F	67	-	NA	-	BMI<30
5 Ctrl	M	57	-	NA	-	BMI<30
6 Ctrl	F	64	-	NA	-	BMI<30
7 Ctrl	F	84	-	NA	-	BMI<30
8 Ctrl	M	84	-	NA	-	180/105/32,4
9 Ctrl	F	73	-	NA	-	165/55/20,2
10 Ctrl	M	69	-	NA	-	170/93/32,1

*BMI – body mass index. NA – data not available.

Supplementary Table S2. qPCR primers and probes for SARS-CoV-2 detection in lung tissue.

Name	Sequence	Label
***N2*-forward**	TTACAAACATTGGCCGCAAA	-
***N2*-reverse**	GCGCGACATTCCGAAGAA	-
***N2*-probe**	ACAATTTGCCCCCAGCGCTTCAG	5'-FAM 3'-BHQ1
***N3*-forward**	GGGAGCCTTGAATACACCAAAA	-
***N3*-reverse**	TGTAGCACGATTGCAGCATTG	-
***N3*-probe**	ATCACATTGGCACCCGCAATCCTG	5'-VIC 3'-BHQ2
***UBC*-forward**	TTGGGTCGCAGTTCTTGTTTG	-
***UBC*-reverse**	TGCCTTGACATTCTCGATGGT	-
***UBC*-probe**	TCGCTGTGATCGTCACTTGACAATG	5'-ROX 3'-BHQ2

*the *N2* and *N3* sequences used were recommended for SARS-CoV-2 detection by Division of Viral Diseases, National Center for Immunization and Respiratory Diseases, Centers for Disease Control and Prevention, Atlanta, GA, USA. *UBC* was added as a reference gene. All oligonucleotides were synthesized by DNK-Sintez (Russia) and put into a triplex one-step qPCR reaction. Sequences are presented in 5′-3′ direction. FAM – fluorescein; VIC – 2′-chloro-7′phenyl-1,4-dichloro-6-carboxy-fluorescein; ROX – carboxyrhodamine; BHQ1/2 – Black Hole Quencher 1/2.

Supplementary Table S3. qPCR primers and probes for the detection of genes of interest in lung tissue.

Name	Sequence	Label
***COX1*-forward**	TTCTTGCTGTTCCTGCTCCT	-
***COX1*-reverse**	TGACAAACTCCCAGAACCAG	-
***COX1*-probe**	CCTTGACCGCTACCAGTGTGA	5'-FAM 3'-BHQ1
***COX2*-forward**	GATGATTGCCCGACTCCCTT	-
***COX2*-reverse**	CTAGCCAGAGTTTCACCGTAA	-
***COX2*-probe**	CCCAGCACTTCACGCATCAGTT	5'-VIC 3'-BHQ2
***UBC*-forward**	TTGGGTCGCAGTTCTTGTTTG	-
***UBC*-reverse**	TGCCTTGACATTCTCGATGGT	-
***UBC*-probe**	TCGCTGTGATCGTCACTTGACAATG	5'-ROX 3'-BHQ2
***LPL*-forward**	GTGCCAGAACTTCGACCCTT	-
***LPL*-reverse**	TTTTCGGAGCCAGAGTTCCC	-
***LPL*-probe**	GATGATCGTGCCTATAAATAGTAG	5'-FAM 3'-BHQ1
***PLA2G4A*-forward**	ATCACACGAACCCAAAGGCA	-
***PLA2G4A* -reverse**	AGCCCAGCATGAAGTTGTGT	-
***PLA2G4A* -probe**	GGTGAGTGATTCAGCTTTATTCAATACC	5'-VIC 3'-BHQ2
***PLA2G2A*-forward**	GGAGTGCAGAACAAACAAGAC	-
***PLA2G2A* -reverse**	GCAGCCGTAGAAGCCATAAC	-
***PLA2G2A* -probe**	ACCATGAAGACCCTCCTACTGTTGG	5'-ROX 3'-BHQ2

* All oligonucleotides were synthesized by DNK-Sintez (Russia) and used in two triplex qPCR reactions (*COX1+COX2+UBC* and *LPL+PLA2G4A+PLA2G2A*) to analyse cDNA obtained from lung tissue. Sequences are presented in 5′-3′ direction. FAM – fluorescein; VIC – 2′-chloro-7′phenyl-1,4-dichloro-6-carboxy-fluorescein; ROX – carboxyrhodamine; BHQ1/2 – Black Hole Quencher 1/2.

Supplementary Table S4. Lipid droplet distribution in lung tissue.

Specimen	Number of frames with:			Total area of lipid droplets, μm^2	
	Intracellular lipid droplets / per 100 frames	Extracellular lipid droplets / per 100 frames	Intra-vessel lipid droplets / per 100 frames	Median / per 20 frames	IQR* / per 20 frames
Non-pneumonia lung 1	30	11	0	39.71	10.26-89.42
Non-pneumonia lung 2	20	11	0	76.57	27.53-131.33
Non-pneumonia lung 3	30	20	0	73.87	31.45-168.94
Non-COVID-19 pneumonia, intact lung 1	65	30	1	327.60	236.26-428.28
Non-COVID-19 pneumonia, intact lung 2	93	12	0	75.95	51.76-270.78
Non-COVID-19 pneumonia, intact lung 3	76	58	0	404.75	199.51-732.86
Non-COVID-19 pneumonia, intact lung 4	69	26	2	162.87	74.32-415.88
Non-COVID-19 pneumonia, inflamed lung 1	96	89	0	1178.58	706.10-1672.91
Non-COVID-19 pneumonia, inflamed lung 2	100	100	18	2930.49	2081.97 - 4549.38
Non-COVID-19 pneumonia, inflamed lung 3	74	67	11	1759.32	642.48-2347.01
Non-COVID-19 pneumonia, inflamed lung 4	68	52	9	506.99	313.01-1559.79
COVID-19 pneumonia, intact lung 1	45	19	1	47.97	2.74-194.60
COVID-19 pneumonia, intact lung 2	90	47	7	348.75	163.46-704.57
COVID-19 pneumonia, intact lung 3	89	41	3	313.58	123.13-773.69
COVID-19 pneumonia, intact lung 4	100	100	0	443.24	261.63-660.08
COVID-19 pneumonia, inflamed lung 1	99	59	5	546.49	107.84 - 1082.08
COVID-19 pneumonia, inflamed lung 2	93	72	18	1236.84	619.31-2516.79
COVID-19 pneumonia, inflamed lung 3	92	58	17	1056.92	235.39-1428.66
COVID-19 pneumonia, inflamed lung 4	100	98	24	2189.44	1415.08 - 2738.02

* IRQ – interquartile range

Supplementary Table S5. **Single-cell RNAseq analysis.**

Cell Type	Tissue	Gene ID	Up/Down
Alveolar type II cells	Lung	*MSMO1*	Upregulated
Alveolar type II cells	Lung	*SCD*	Upregulated
Alveolar type II cells	Lung	*FDFT1*	Upregulated
Alveolar type II cells	Lung	*HMGCS1*	Upregulated
Alveolar type II cells	Lung	*FASN*	Upregulated
Fibroblasts	Lung	*FGF2*	Downregulated
Fibroblasts	Lung	*RARRES2*	Downregulated
Fibroblasts	Lung	*DKK3*	Downregulated
Fibroblasts	Lung	*PDGFRA*	Downregulated
Fibroblasts	Lung	*FGFR4*	Downregulated
Endothelial cells	Lung	*FLT1*	Upregulated
Endothelial cells	Lung	*RELN*	Upregulated
Endothelial cells	Lung	*PIK3R3*	Downregulated
Endothelial cells	Lung	*PDGFB*	Downregulated
Endothelial cells	Lung	*FGF2*	Downregulated
Macrophage	Lung	*PSAP*	Upregulated
Macrophage	Lung	*SPP1*	Upregulated
Macrophage	Lung	*GLUL*	Upregulated
Macrophage	Lung	*FABP4*	Downregulated
Macrophage	Lung	*RBP4*	Downregulated
Macrophage	Lung	*RETN*	Downregulated
Macrophage	Lung	*INHBA*	Downregulated
Macrophage	Lung	*PPARG*	Downregulated
Macrophage	Lung	*FFAR4*	Downregulated
Macrophage	Lung	*LPL*	Downregulated
Macrophage	Lung	*FABP3*	Downregulated
Macrophage	Lung	*NMB*	Downregulated
Macrophage	Lung	*ADTRP*	Downregulated
Macrophage	Lung	*AKR1C2*	Downregulated
Macrophage	Lung	*SCD*	Downregulated
Macrophage	Lung	*AKR1C3*	Downregulated
Monocytes	Lung	*ABHD5*	Upregulated
Monocytes	Lung	*G0S2*	Upregulated
Monocytes	Lung	*HCAR2*	Upregulated
Monocytes	Lung	*ANXA2*	Downregulated
Monocytes	Lung	*THBS1*	Downregulated
T cells	Lung	*IFNG*	Upregulated
T cells	Lung	*FYN*	Upregulated
T cells	Lung	*CCL5*	Upregulated
T cells	Lung	*LIPA*	Downregulated
T cells	Lung	*FUCA1*	Downregulated
T cells	Lung	*APOE*	Downregulated
T cells	Lung	*APOC1*	Downregulated
T cells	Lung	*APOC2*	Downregulated
T cells	Lung	*PLTP*	Downregulated
T cells	Lung	*FABP3*	Downregulated

T cells	Lung	*FABP4*	Downregulated
T cells	Lung	*SCD*	Downregulated

* The tissue type in analysis was restricted to “Lung” and the cell types in analysis were restricted to the most prominent resident/infiltrating cell populations. The genes showing controversial results in different datasets were excluded. In the lung tissue, the downregulated genes prevail, most notably in fibroblasts, macrophages and T-cells.